

CO₂ Methanation on Cu-Cluster Decorated Zirconia Supports with Different Morphology: A Combined Experimental In Situ GIXANES/GISAXS, Ex Situ XPS and Theoretical DFT Study

Avik Halder,[◆] Cristina Lenardi,[◆] Janis Timoshenko,[◆] Antonija Mravak,[◆] Bing Yang, Lakshmi K Kolipaka, Claudio Piazzoni, Sönke Seifert, Vlasta Bonačić-Koutecký, Anatoly I. Frenkel, Paolo Milani,* and Stefan Vajda*



Cite This: *ACS Catal.* 2021, 11, 6210–6224



Read Online

ACCESS |



Metrics & More



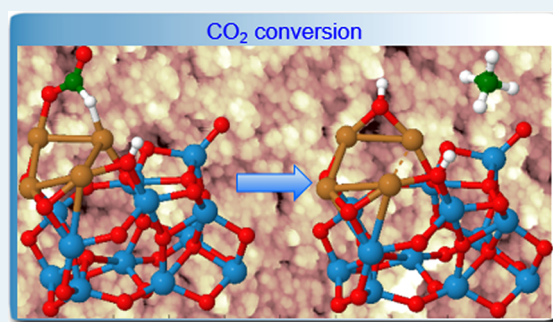
Article Recommendations



Supporting Information

ABSTRACT: Subnanometer copper tetramer–zirconia catalysts turn out to be highly efficient for CO₂ hydrogenation and its conversion to methane. The cluster size and substrate morphology are controlled to optimize the catalytic performance. The two types of zirconia supports investigated are prepared by atomic layer deposition (~3 nm thick film) and supersonic cluster beam deposition (nanostructured film, ~100 nm thick). The substrate plays a crucial role in determining the activity of the catalyst as well as its cyclability over repeated thermal ramps. A temperature-programmed reaction combined with in situ X-ray characterization reveals the correlation between the evolution in the oxidation state and catalytic activity. Ex situ photoelectron spectroscopy indicates Cu clusters with stronger interactions with the nanostructured film, which can be the cause for the higher activity of this catalyst. Density functional theory calculations based on the Cu₄O₂ cluster supported on a ZrO_x subunit reveal low activation barriers and provide mechanism for CO₂ hydrogenation and its conversion to methane. Altogether, the results show a new way to tune the catalytic activity of CO₂ hydrogenation catalysts through controlling the morphology of the support at the nanoscale.

KEYWORDS: CO₂ conversion, copper cluster, support effect, reaction mechanism, XANES, GISAXS, XPS, DFT



INTRODUCTION

Catalytic conversion of CO₂ to useful fuels such as methane, methanol, and longer chain hydrocarbons can help to simultaneously mitigate the emission of greenhouse gas CO₂ and enrich the resource of chemical feedstock compounds to reduce the dependency on fossil fuels.^{1,2} The interest in developing cheap catalyst with optimized performance is obvious and Cu based catalysts have already been heavily explored.^{2,3} However, in most cases one has to use high pressure and temperature as the reaction conditions to achieve high conversion efficiency for CO₂ at the industrial level.^{4–6} There has recently been reports of highly efficient conversion of CO₂ to methanol using Cu cluster based catalysts (Cu_n deposited on hydroxylated alumina supports) at temperatures as low as 125 °C and 1.1 atm pressure. However, the methane signal appeared only at temperatures of around 375 °C^{7,8} also observed during the course of reaction dynamically forming and disintegrating nanoassemblies made of subnanometer Cu clusters.⁹ Iron oxide doped with Cu nanoparticles on the other hand was found to have a high selectivity for CO₂ hydrogenation with methane as the major usable product.¹⁰

Zirconia supports have been of interest due to their high mechanical and thermal stability, and the copper/zirconia catalyst was found to be a stable catalyst for conversion of syngas to methanol.^{11,12} Some of the commonly used Cu/zirconia catalysts for CO₂ conversion include copper and copper oxides mixed with microcrystalline zirconia present in amorphous, tetragonal, or monoclinic phases,^{13–16} carbon nanofiber based Cu/zirconia catalyst,¹⁷ and copper nanocrystals encapsulated in Zr based metal–organic frameworks.¹⁸ Herein we prepared a catalyst with monodisperse Cu clusters supported on zirconia substrates prepared by two different deposition methods. The first method, atomic layer deposition¹⁹ (ALD ZrO_x) creates a smooth zirconia surface which is about 3 nm thick. The second method, supersonic cluster deposition (SCBD), fabricates

Received: November 17, 2020

Revised: February 12, 2021

cluster-assembled nanostructured zirconia films of 100 nm in thickness (NS ZrOx).^{20,21}

SCBD produces nanostructured films with nanoscale topography and roughness that can be quantitatively controlled over a wide interval of parameters:²⁰ the morphology of cluster-assembled materials is characterized by arrangements of nanoscale building blocks in larger units up to a certain critical length scale determined by the time of the deposition process.²¹ Cluster-assembled zirconia films are characterized by high specific area and porosity at the nano- and subnanometer scales.^{20,21} Cluster-assembled zirconia substrates are rich in undercoordinated defects,²⁰ very stable against thermal treatments and have high surface area.²² These aspects make cluster-assembled zirconia a very interesting catalytic substrate where the effect of metallic cluster decoration can be investigated.²³

The copper clusters were created with atomic precision. Such systems have the capability to perform catalytic reactions with high activity and selectivity; hence, one can determine the most active catalytic moiety.^{24,25} In the present study Cu_n/zirconia catalysts were investigated in search for an efficient catalyst for CO₂ methanation. Methane forms a major source of stored energy and is usually produced using complex processes at high temperature and under high pressure^{26,27} or extracted from natural sources.^{28–32} Thus, an affordable catalyst which can produce methane by conversion of CO₂ is highly desirable.

Pure Cu clusters of controlled atomicity were generated in a high vacuum system, free of any ligands and deposited on zirconia substrates with different morphologies. Using X-ray photoelectron spectroscopy (XPS) the binding energies of the clusters on zirconia surfaces have been measured. The temperature-programmed reaction with mass spectroscopic detection was used to monitor the evolution of the products in real time, where the changes in the composition and oxidation state of copper during the reaction were monitored using in situ grazing incidence X-ray absorption near-edge spectroscopy (GIXANES). Simultaneous in situ grazing incidence small-angle X-ray scattering (GISAXS) was employed to check for any assembly formation or coalescence of clusters. The analysis of oxidation states and structures of metal clusters in reaction conditions was performed by spectral decomposition of GIXANES data.

In order to understand the role of the copper cluster and support, DFT calculations have been carried out on a model reactive center formed by oxidized copper tetramer and Zr_xO_{2x} subunit, providing energy profile and identifying key steps of the mechanism, thus proposing energetically favorable reaction pathway during the activation and hydrogenation steps of CO₂ on route to its conversion to methane.

EXPERIMENTAL SECTION

Design of ALD and Nanostructured Zirconia Supports.

The ALD ZrOx support was prepared using tetrakis-(dimethylamido)zirconium(IV) (ZrTDMA) precursor purchased from Aldrich. The film was deposited at a reactor temperature of 200 °C with the manifold at 150 °C. ZrTDMA (75 °C) and deionized water were used for the growth of ZrO₂, with a pulsing sequence of 0.4–10–0.015–10 s.¹⁹

Nanostructured zirconia (NS ZrOx) thin films were produced using a supersonic cluster beam deposition (SCBD) apparatus equipped with a Pulsed Microplasma Cluster Source (PMCS)³³ as described in detail in refs 20 and 21. In brief, the deposition apparatus consists of two differentially pumped vacuum stages. A PMCS is mounted outside the first chamber (expansion

chamber) on the axis of the apparatus. The PMCS is operated in a pulsed regime: high-pressure Ar pulses with a duration of a few hundreds of microseconds are injected at the repetition rate of 4 Hz. The gas injection is followed by an electrical discharge between the cathode (zirconium rod) and an anode buried in the source body. A subsequent condensation of sputtered atoms results in cluster nucleation. The inert gas-clusters mixture is then extracted from the PMCS into high vacuum ($p \approx 10^{-6}$ mbar) to form a seeded supersonic cluster beam. Cluster deposition takes place in the deposition chamber where the supersonic beam impinges on silicon substrates mounted on a *x-y-z* motorized sample holder.

In the PMCS metallic Zr clusters are produced. Nevertheless, a substantial oxidation of the clusters takes place very rapidly because of the interaction of the Zr clusters with oxygen and water molecules, upon exposure of the sample to air, resulting in cluster-assembled nanostructured ZrOx films (NS ZrOx) with $x \approx 2$.

We characterized by atomic force microscopy (AFM) the evolution of the samples morphological properties as a function of the surface coverage, which is defined as the ratio between the projected area occupied by clusters on the surface and the scanned area.²⁰ Nanostructured films with a thickness of 125 nm and roughness of 17 nm (see Figure S1) were grown under the ballistic deposition regime where clusters stick on the substrate upon landing without significant mobility and fragmentation due to their low kinetic energy.²¹ The NS ZrOx film was characterized by the BET method obtaining a specific surface area of approximately 300 m²/g and nanosized pores with sizes in the range of 10–50 nm.²²

Copper Cluster Deposition. Cu clusters were produced in a liquid nitrogen cooled magnetron sputtering source, the details for which can be found in Supporting Information and in ref 34. Briefly, the clusters were produced in a magnetron sputtering source (Figure S2) and the clusters of desired single size were mass-selected from the molecular beam and soft-landed on the ALD and NS ZrOx supports at controlled loading of copper metal. The copper loading per cluster spot in these samples was about 5 ng, corresponding to 4.45×10^{13} Cu atoms.

In Situ GIXANES, GISAXS, and TPRx. The testing of performance and characterization of the working catalyst was performed in a home-built reactor at beamline 12-ID-C of the Advanced Photon Source at the Argonne National Laboratory.³⁵ This experimental setup allows in situ X-ray monitoring of changes in the size of the clusters by small-angle X-ray scattering at grazing incidence (GISAXS) and to follow the changes in the oxidation state of the metal by grazing incidence X-ray absorption near edge spectroscopy with fluorescence mode detection (GIXANES), as well as to simultaneously monitor reaction product formation during a temperature-programmed reaction (TPRx). A brief description of the multiprobe approach is given in the Supporting Information and in detail elsewhere.^{35,36} The reaction was performed using a uniform double heat and cool ramp (see the Results and Discussion section), at a pressure of 1.1 atm under continuous flow of 18 sccm of pure CO₂ and H₂ in 1:3 ratio.

The spectra of the Cu metal foil, Cu₂O, CuO, and Cu(OH)₂ bulk standards were collected at the 12-BM beamline of the Advanced Photon Source in transmission mode. These spectra were used as reference spectra for linear combination fit (LCF) analysis of the XANES spectra. Note here that the local structure in ultrasmall clusters deviates from that in the bulk materials such as the standards used in this study. Therefore, in this work

(a) Temperature ramp

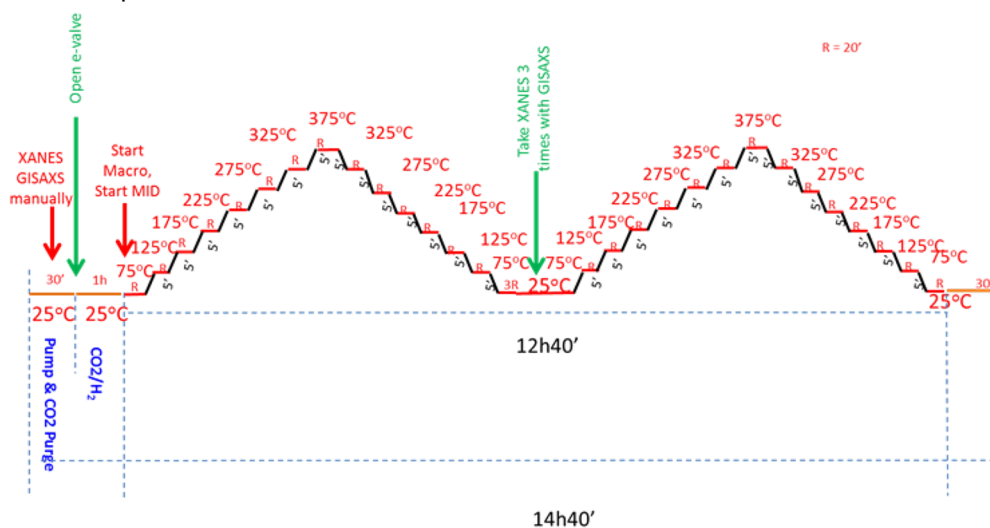
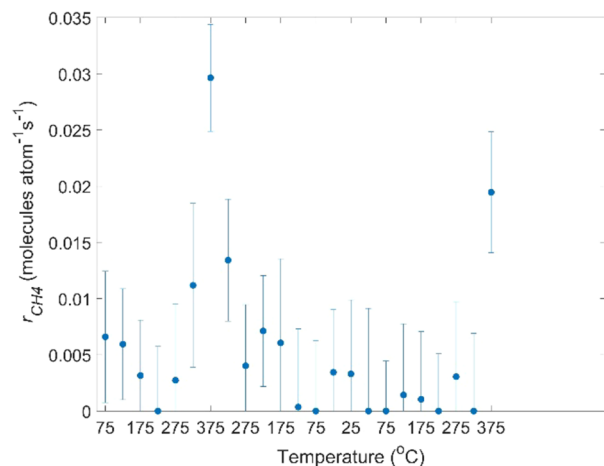
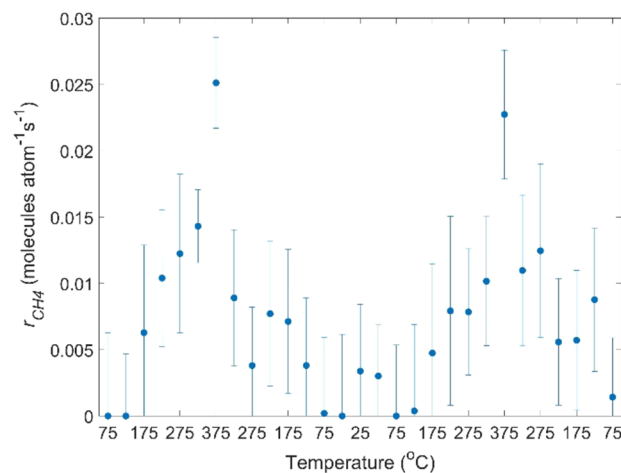
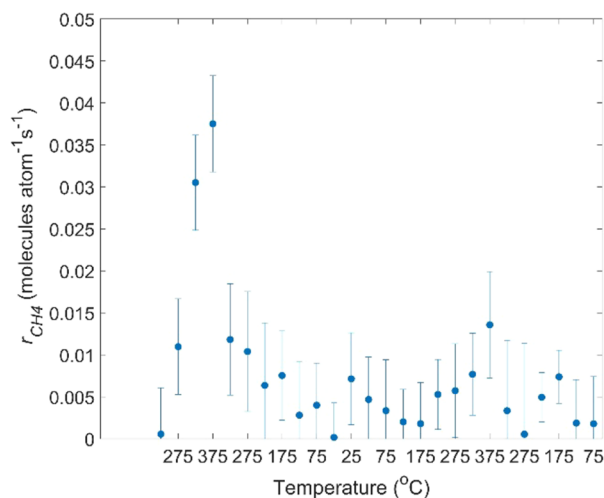
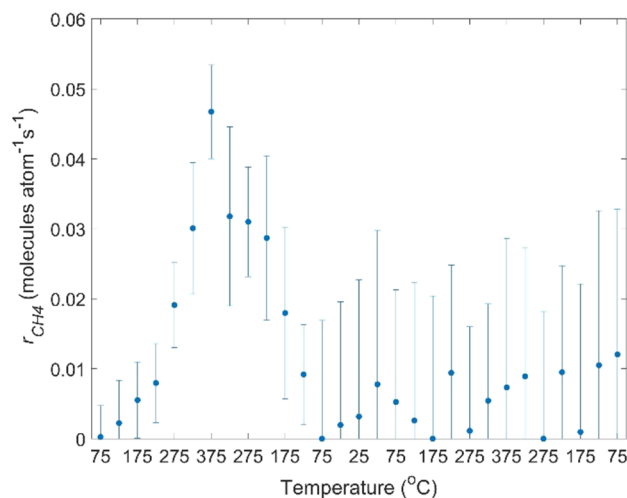
(b) Cu₄ on ALD ZrOx(c) Cu₁₂ on ALD ZrOx(d) Cu₄ on NS ZrOx(e) Cu₁₂ on NS ZrOx

Figure 1. Catalytic activity of Cu₄ and Cu₁₂ clusters on ALD ZrOx and NS ZrOx. (a) Temperature ramp; (b) Cu₄ on ALD zirconia with a reproducible activity for methane formation from CO₂ on consecutive ramps; (c) Cu₁₂ on ALD zirconia with a reproducible activity for methane formation from CO₂ on consecutive ramps; (d) Cu₄ on NS ZrOx with a activity for methane formation from CO₂ significantly decreased during the second ramp; and (e) Cu₁₂ on NS ZrOx with a activity for methane formation from CO₂ quenched during second ramp.

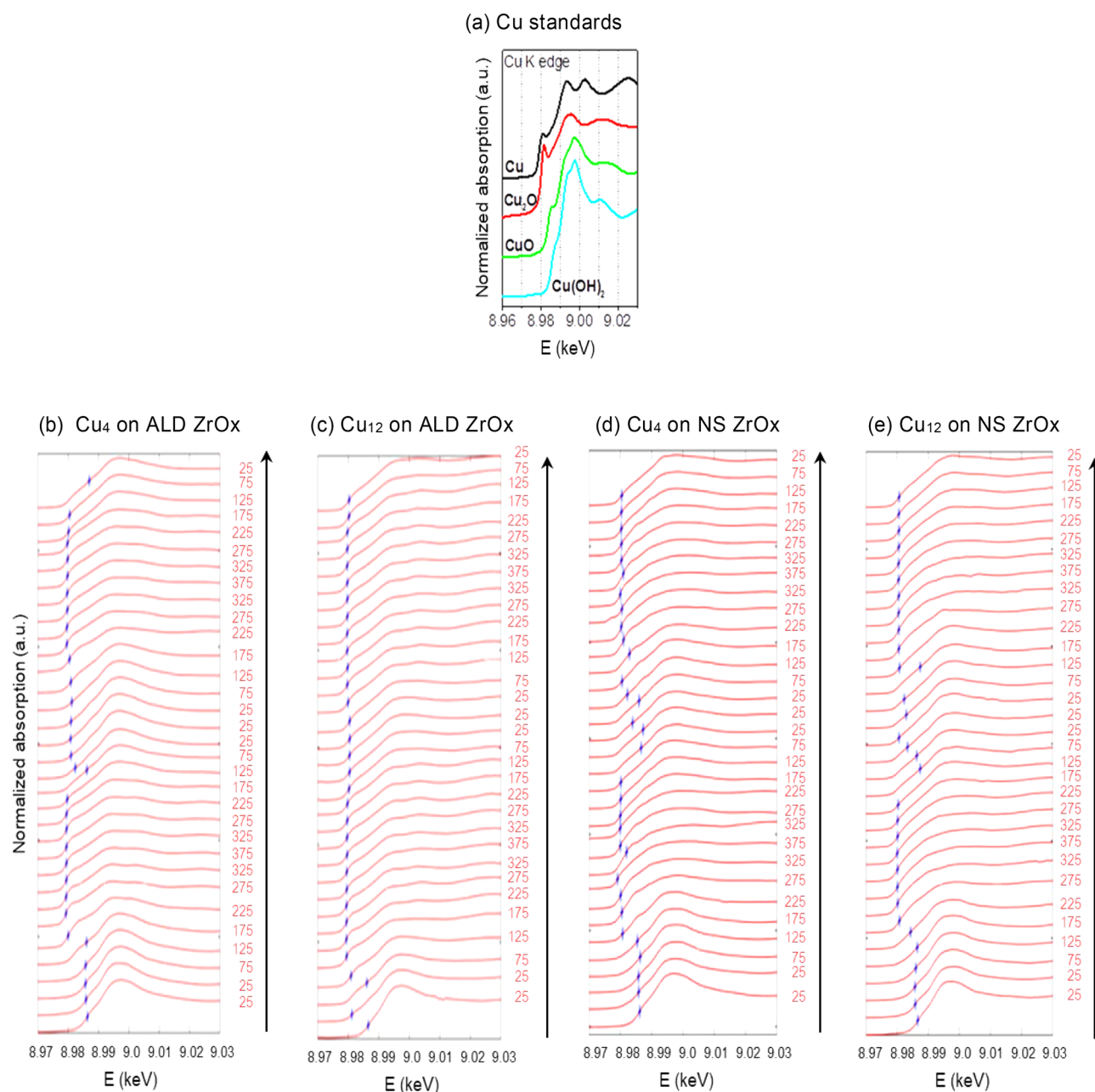


Figure 2. XANES spectra collected at the Cu K-edge during the double ramp shown in Figure 1a. (a) Cu bulk standards; (b) Cu₄ on ALD ZrOx; (c) Cu₁₂ on ALD ZrOx; (d) Cu₄ on NS ZrOx; and (e) Cu₁₂ on NS ZrOx. The blue bar in the plots indicates the position of the edge of the spectra, calculated by the location of the first peak of the derivative in the XANES spectra. It is shifted toward lower or higher energies, indicating the change in the oxidation state to the lower or higher values, respectively.

we complement the LCF approach by a multivariate curve resolution - alternating least squares (MCR-ALS) method,³⁷ which has proven to be instrumental for speciation of mixtures, when the exact reference spectra for pure components are not known.

Using an X-ray beam of 9.1 keV energy, 2-dimensional GISAXS images were collected to monitor possible agglomeration of Cu clusters during the reaction can be obtained^{35,38–40} and the scattering patterns were analyzed with the Modeling II tool in the Irena tool suite.⁴¹

GIXANES Spectra Analysis. GIXANES data were analyzed to obtain the changes in the oxidation state of the clusters using two different techniques:

LCF Technique. The Cu clusters XANES spectra were fitted as a linear combination of bulk Cu standard XANES spectra, Cu (Cu⁰), Cu₂O (Cu⁺), CuO (Cu²⁺), and Cu(OH)₂ (Cu²⁺). The spectra were processed by using a linear least-squares optimization algorithm, which provides the contributions from individual motifs to the ensemble-average spectrum of the clusters.^{42,43} (see Figure S3) By performing LCF analysis for spectra collected at all temperatures, one can obtain the evolution of unique subsets of clusters during the reaction can be obtained. This method assumes prior knowledge of the standards and requires independent validation that the standards adequately represent the states of the clusters in reaction condition.

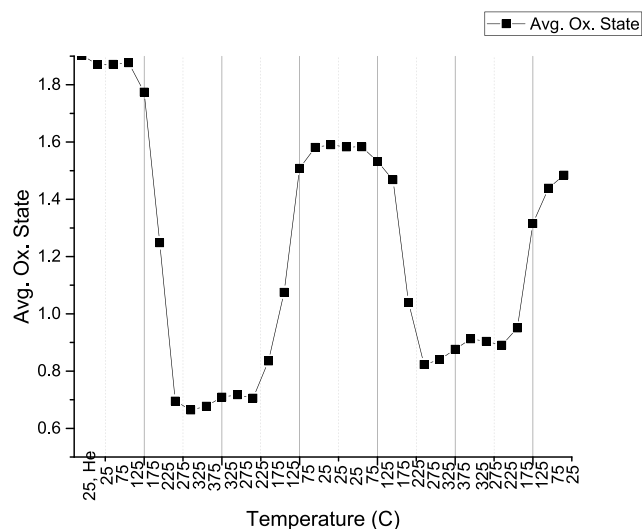
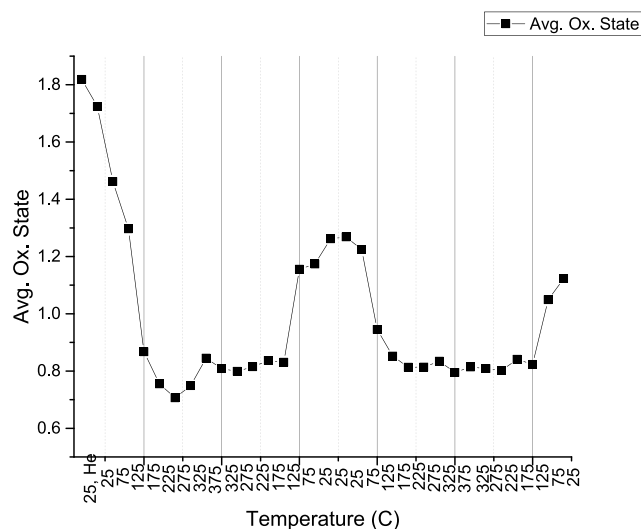
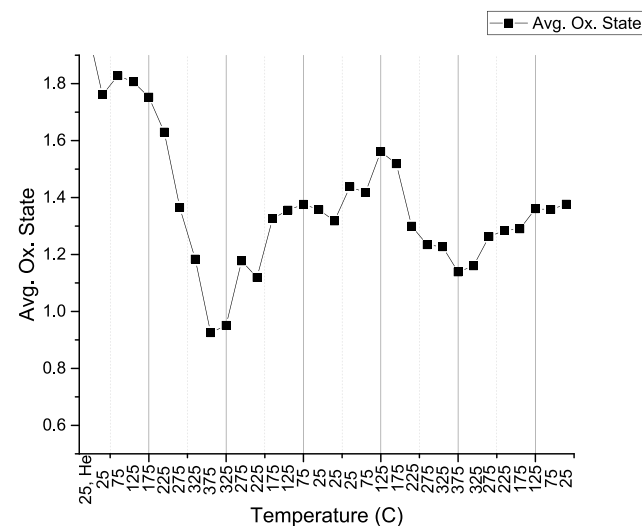
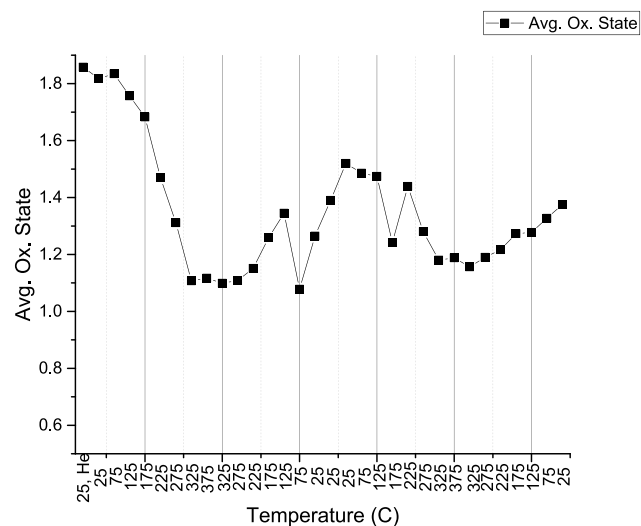
(a) Cu₄ on ALD ZrOx(b) Cu₁₂ on ALD ZrOx(c) Cu₄ on NS ZrOx(d) Cu₁₂ on NS ZrOx

Figure 3. Evolution of oxidation state of copper in the clusters during the reaction, from LCF fitting of XANES spectra and corresponding compositions shown in Figure S3. (a) Cu₄ on ALD ZrOx; (b) Cu₁₂ on ALD ZrOx; (c) Cu₄ on NS ZrOx; and (d) Cu₁₂ on NS ZrOx.

MCR-ALS Technique. The accuracy of the LCF approach discussed above can be limited by the fact that the local structure of nanostructured materials and hence their X-ray absorption spectra can be quite different from those in corresponding bulk materials. In the MCR-ALS approach, in turn, the spectra corresponding to pure compounds (which are not known a priori for nanosized materials) are determined automatically from the series of experimental data for mixtures. The MCR-ALS method and its application to XANES data analysis are discussed in refs 37 and 44–48. In particular, ref 46 is a good example of application of the MCR-ALS method for identification of different species in copper-based nanocatalysts from temperature-dependent Cu K-edge XANES data and demonstrates clearly the limitations of the LCF technique. For example, it was shown that LCF may severely overestimate contribution of Cu⁺ species in the speciation of nanosized copper catalysts.⁴⁶ Briefly, MCR-ALS method is applicable if a set of experimental XANES spectra μ_i is available, where each

spectrum can be expressed as a linear combination of a few spectra s_j that correspond to pure compounds, weighted by w_{ij} : $\mu_i(E) = \sum_j w_{ij} s_j(E)$. Using matrix notation, this set of equations can be rewritten as $M = WS$, where the matrices M , W , and S are formed from experimental spectra $\mu_i(E)$, weights w_{ij} and spectra for pure compounds $s_j(E)$, correspondingly. To obtain unique results for W and S , the following constraints are imposed: 1) all elements of matrices W and S should be non-negative and 2) $\sum_j w_{ij} = 1$. Elements of W and S are then refined in an iterative process. One starts with a rough initial estimation of matrix W (in our case, the initial guesses of concentration profiles can be obtained from the conventional LCF analysis). To obtain the initial approximations of spectra for pure compounds, linear least-squares problem is then solved with respect to S to minimize the norm $\|M - WS\|$. Next, elements of matrix W are similarly updated, by solving least-squares problem with respect to W and taking into account the above-mentioned constraints. The process is repeated until there is no more significant

reduction of the norm $\|M - WS\|$. If the initial guess of matrix W is not too far from the true values, MCR-ALS method is able to recover the spectra for pure compounds, as well as the weights of the pure compounds spectra in each of the experimentally acquired spectrum (see Figure S4). To illustrate and validate the MCR-ALS method for the analysis of Cu K-edge XANES data, in the Supporting Information, Figure S6, we apply it to analyze a set of model data, constructed as artificial linear combinations of experimental XANES for bulk reference compounds: metallic copper, Cu_2O , CuO , and $\text{Cu}(\text{OH})_2$. As shown in Figure S7, the MCR-ALS method in this case is able to reconstruct quite reliably all four reference spectra and also their contributions to each of the mixtures.

Importantly, as part of the MCR-ALS analysis procedure, we have also verified that two components should be sufficient to describe experimental data for each of the samples by using principal component analysis (PCA).^{49–51}

XPS Analysis. The XPS measurements were performed with a Leybold LHS 10/12 UHV apparatus equipped with a hemispherical electron analyzer and a conventional X-ray source ($\text{Mg K}\alpha = 1253.6 \text{ eV}$). The high resolution spectra were acquired in the constant step energy mode with $E_{\text{pass}} = 30 \text{ eV}$. The overall energy resolution was 0.8 eV . The pressure in the experimental chamber during experiments was below $6 \times 10^{-9} \text{ mbar}$. The binding energy scale of the spectrometer was calibrated via the Au $4f_{7/2}$ core level line (located at 83.97 eV) of a clean polycrystalline Au sample. Due to the moderate charging in all of the analyzed samples and considering that the substrates are all zirconium oxide, the spectra were aligned by using as reference the adventitious carbon peak conventionally positioned at 284.8 eV . The spectra were fitted with a Shirley background or with linear background that was subsequently removed for zirconium and oxygen spectra. The oxygen and zirconium spectra were fitted with a linear combination of Gaussian and Lorentzian line-shapes with larger weight of the Gaussian component. The least-squares curve-fitting were performed with the code WinSpec, developed at the LISE laboratory, Namur, Belgium.

RESULTS AND DISCUSSION

Cu clusters on both ALD coated and nanostructured zirconia were found to be highly active and selective toward methane production. The reaction was performed using a uniform double heat and cool ramp (Figure 1a), at a pressure of 1.1 atm under continuous flow of 18 sccm of pure CO_2 and H_2 in 1:3 ratio. An initial look at the reactivity data (reaction rates) can be summarized as follows. During the first ramp, the activity of $\text{Cu}_4/\text{NS ZrOx}$ was found to be approximately 30% higher than that of $\text{Cu}_4/\text{ALD ZrOx}$, and the activity of $\text{Cu}_{12}/\text{NS ZrOx}$ was approximately twice that of the activity of $\text{Cu}_{12}/\text{ALD ZrOx}$. However, the activity of $\text{Cu}_{12}/\text{NS ZrOx}$ drops over a repeated cycle, as discussed below.

The comparison of activity and X-ray results revealed a strong correlation between the activity and oxidation state of the clusters:

Cu Clusters on ALD ZrOx. The spectra of the Cu metal foil, Cu_2O , CuO , and $\text{Cu}(\text{OH})_2$ used as bulk standards are shown in Figure 2a. The spectrum of copper in Cu_4 clusters supported on ALD ZrOx indicate a $\text{Cu}(\text{OH})_2$ -like structure at room temperature, as deduced from XANES spectrum collected under flowing He before the beginning of the heating ramp (Figure 2b). The evolution of the oxidation state of copper in the

Cu_4 and Cu_{12} cluster during the applied temperature ramp obtained from LCF analysis is shown in Figure 3a,b, respectively

XPS characterization was carried out ex situ before and after the complete thermal treatment. Figure 4 shows the high

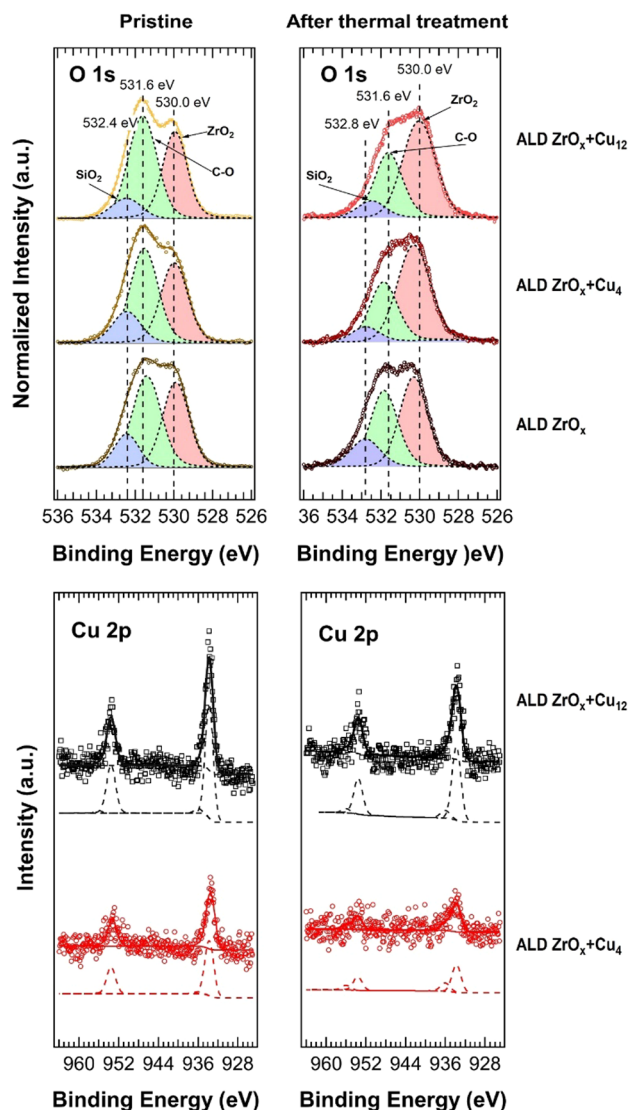


Figure 4. XPS spectra of pristine and after the complete thermal process of ALD ZrO_x samples. Upper panels: fitted normalized O 1s spectra; bottom panels: fitted Cu 2p spectra.

resolution XPS spectra and the peak fitting of O 1s edges of the ALD ZrO_x , namely the pristine sample and the sample after the thermal treatment without and with the Cu_4 and Cu_{12} clusters.

Figure S4 shows the corresponding Zr 3d spectra. The fwhm of the Zr 3d peaks is about 1.5 eV . The Zr 3d $5/2$ peak is found at 182.0 eV with spin–orbit splitting of 2.3 eV . This BE could be referred to oxygen-deficient zirconia (ZrO_{2-x}), as also assessed by the evaluation of the stoichiometry obtained by the ratio between the area of Zr 3d peak and the area of the fitted oxygen peak corresponding to the lattice oxygen (Zr^{4+}) centered at 530.0 eV (red filled peaks in Figure 4, upper panels). The complete thermal process promotes the oxidation of zirconium. In O 1s spectra the feature centered at 531.6 eV (green filled peaks in Figure 4) is related to the contribution of oxygen bonded to carbon in organic species and oxygen bonded to zirconium but with no lattice occupancy that is either an

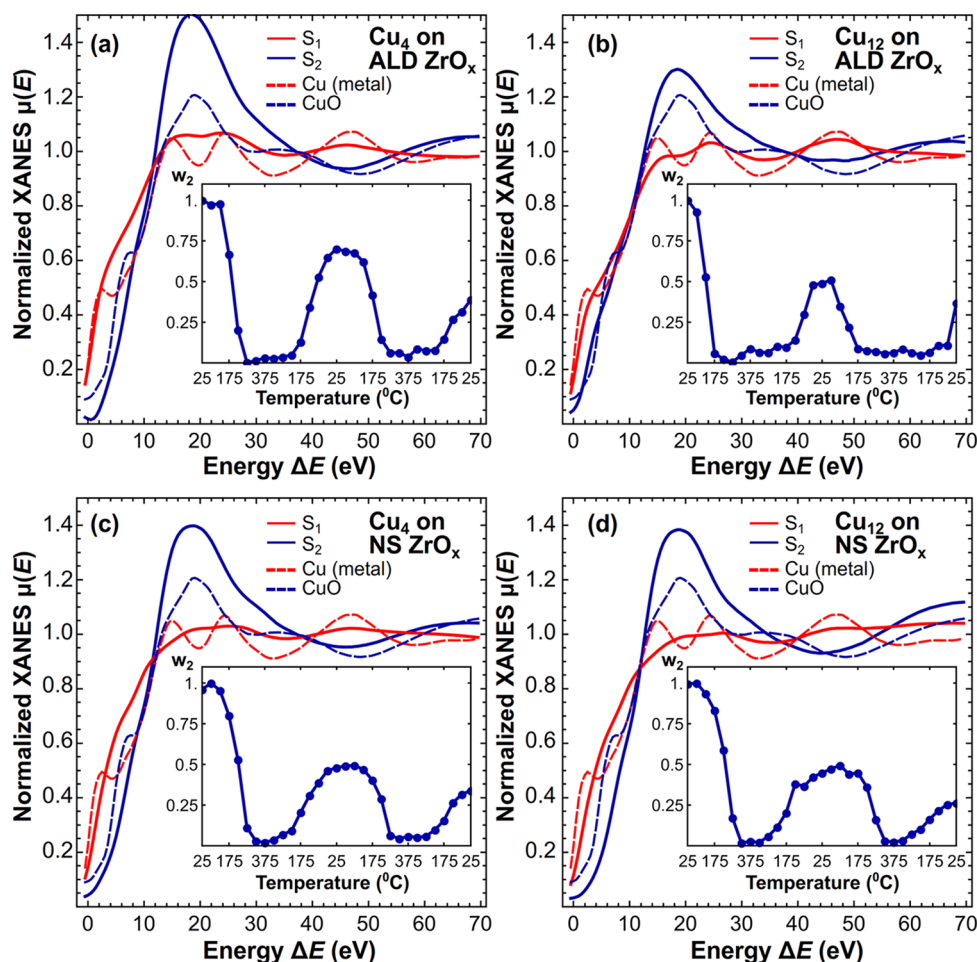


Figure 5. Evolution of Cu cluster composition during the reaction as obtained from MCR-ALS analysis for Cu_4 on ALD ZrO_x (a), Cu_{12} on ALD ZrO_x (b), Cu_4 on NS ZrO_x (c), and Cu_{12} on NS ZrO_x (d). XANES spectra S_1 and S_2 for two species identified by the MCR-ALS method are shown as solid lines and compared with experimental spectra for bulk reference materials (metallic Cu and CuO, dashed lines). Temperature-dependencies of the weight of contribution of S_2 (which resembles the spectrum for oxide) to the total spectra are shown in the insets.

indication of oxygen vacancies and a certain degree of surface hydroxylation of the support.^{52,53} The possible contribution of copper oxides should also be in the BE region between 529.5 and 530.5 eV but, due to the low content of the element, its amount is expected to be negligible with respect to the exceeding O–Zr contribution and no reliable deconvolution of the two metal oxides can then be performed. In O 1s spectra silicon dioxide is also detected (blue filled peak at 532.4 eV). Its contribution comes from the support on which the thin ALD zirconia film was deposited in accordance with the intense silicon peak observed in the wide spectrum (not shown). In Zr 3d and O 1s spectra no evident features ascribable to the presence of copper clusters arise. Figure 4 (bottom panel) shows the Cu 2p peaks of the ALD ZrO_x samples before and after the complete thermal process. All of the samples show the main Cu $2p_{3/2}$ at 933.7 eV with a spin orbit splitting of 20.0 eV. The peak position and the narrow shape of the $2p_{3/2}$ peaks of the pristine samples are strong indications that Cu is mainly in metallic form (Cu(0)) or in oxidation state Cu(I) since these two contributions are not easily distinguishable, according to the reference spectra of copper oxides reported by Pauly et al.⁵⁴ The component Cu(II), identified via a small fitting peak at higher BE,⁵⁴ is negligible for the pristine sample.

The catalyst changes its composition drastically when heated in the presence of CO_2 and H_2 . Indeed, above 175 °C the Cu_2O

and CuO phase appear (see Figure S3a). At 275 °C the composition further changed to a mixture of Cu_2O and metallic Cu with contributions of 70% and 30%, respectively. Note, however, that, as demonstrated in ref 46, the significant contribution of Cu_2O at high temperatures may be an artifact of the LCF procedure in this case. The composition remained constant as the clusters were heated up to 375 °C. The oxidation state dropped from +2 at room temperature to 0.7 at 225 °C and was stable at higher temperatures. The changes of the composition and oxidation state of copper were reversible as seen from the cool-down ramp. The oxidation state started to increase when the samples were cooled below 225 °C and rose to 1.6 at room temperature. The changes in the oxidation state were identical in the next cycle. MCR-ALS results for Cu_4 clusters on ALD zirconia are shown in Figure 5a and are in qualitative agreement with LCF results discussed below. Two components (S_1 and S_2) were identified, such that experimental spectra, acquired at different temperatures, can be expressed as linear combinations of S_1 and S_2 . The representative fits of experimental XANES spectra with linear combinations of S_1 and S_2 are shown in the Supporting Information, Figure S7. Nearly perfect MCR-ALS fit indicates that two components are sufficient to describe the whole experimental data set. Existence of additional species cannot be ruled out completely, but they need to be either extremely short-lived (i.e., contributing to a

single experimental spectrum only), or their concentration should be completely correlated with the concentration of some other species. By comparing the spectral components, yielded by MCR-ALS technique, with the spectra of reference compounds (Supporting Information, Figure S5), one can conclude that component S_1 corresponds to metallic copper, while component S_2 can be associated with a spectrum of oxidized copper species. At the same time, one can see clearly the differences between S_1 and S_2 and XANES data for bulk reference compounds. In particular, one can note that the spectrum for metallic species (S_1) has much broader, smoother features than XANES for bulk metallic copper, as expected for metallic clusters of very small size.^{46,55} The observed differences between S_1 and S_2 and XANES data for bulk references is a warning sign that conventional LCF may be inaccurate in this case,⁴⁶ and there is a need for a complementary MCR-ALS approach. The temperature dependence of the weight of the S_2 component, which can be associated with the fraction of oxidized Cu species, is shown in the inset in Figure 5a. The as-prepared Cu_4 sample on ALD zirconia sample is nearly completely oxidized, and preserves its state up to ca. 150 °C. Upon further temperature increase, the sample is rapidly reduced, and is almost completely metallic at 225 °C. The fact that MCR-ALS suggests that the sample is reduced almost completely is the main difference between MCR-ALS and LCF results. As mentioned above, this difference can be explained by the known artifact of the LCF procedure for nanosized catalysts.⁴⁶ Upon subsequent cooling, the sample is partially reoxidized. Similarly to the conclusions made on the basis of the LCF analysis, MCR-ALS suggests that reoxidation occurs sharply when the temperature falls below 225–175 °C.

The activity of the catalyst followed from the measured TPRx signal showed highest activity for methane ($m/z = 15$) production, whereas no detectable signal was seen for methanol ($m/z = 31$). Methane production started at 275 °C and peaked at 375 °C with r_{CH_4} of 0.03 molecules atom⁻¹ s⁻¹ as shown in Figure 1b for Cu_4 on ALD ZrOx. It was also found that the activity measured during the slow heat and cooling ramps is symmetric which shows that there is no deactivation of the catalyst by the heating to a high temperature. The catalyst is cycled for two consecutive ramps with a 90 min rest at room temperature in between the two ramps. The sample with Cu_4 clusters in the second ramp lost about 30% of its activity, for which we have no unambiguous explanation. We speculate that this drop could be caused due to changes in the ALD ZrOx support and clusters getting partially embedded into the support.

The XANES spectra measured under He for the Cu_{12} clusters showed that copper in the clusters was present as $\text{Cu}(\text{OH})_2$ similar to Cu_4 clusters as seen in Figures 2c and S3b, respectively. However, the changes observed in the Cu_{12} clusters exhibited a more gradual pattern as the oxidation state of copper started dropping as soon as the reactant gases were introduced within the reactor. As seen from Figures 2c and 3b the oxidation state of the clusters dropped to 0.8 above 175 °C and did not change while the clusters are heated up to 375 °C and also during cooling until 175 °C. On further cooling to room temperature the oxidation state increased to 1.2. The change in the oxidation state occurred in the same manner in the following cycle. The final oxidation state for copper in the dodecamer clusters at 375 °C was the same; however, the clusters were composed of about 50% metallic Cu and the rest of the

composition was in an oxidized state. The changes in the composition were reproducible over the two consecutive ramps.

In XPS (see Figure 4), after the thermal process the detected Cu 2p signal shows a larger spread. The fit highlights a more intense peak arising at higher BE, attributable to an increased amount of the Cu(II) phase, more evident for the samples with Cu_4 clusters. The reduction in peak intensities with respect to pristine sample can be mainly attributed to the diffusion of the copper clusters in/on the zirconia support.

MCR-ALS results for Cu_{12} clusters on ALD ZrOx (Figure 5b) are, again, in qualitative agreement with LCF results and also suggest a more gradual initial reduction compared to the Cu_4 sample. At the same time, the completely reduced state was reached faster, at lower temperature (175 °C for Cu_{12} clusters in comparison to 225 °C for Cu_4) clusters. This may explain the differences in catalytic properties for these systems, vide infra. Upon consequent cooling, the Cu_{12} sample was also reoxidized to a lesser degree than the Cu_4 sample, in agreement with LCF. We note that, following a similar procedure in analyzing experimental XANES data for both Cu_4 and Cu_{12} clusters (spectra for each of the samples were analyzed separately), we have found that MCR-ALS decomposition of experimental spectra into mixtures of two components is able to reproduce reasonably experimental spectra for all samples, and inclusion of the third component in the analysis does not improve results significantly.

Cu_{12} clusters were active at temperatures as low 175 °C, which is about 100 °C lower than the onset temperature seen for Cu_4 clusters. This temperature is lower than any of the previously reported catalysts in literature and at atmospheric pressure.^{56–60} r_{CH_4} reaches 0.025 molecules atom⁻¹ s⁻¹ at 375 °C during the first ramp and maintains about 90% of its activity during the second cycle which makes Cu_{12} as one of the most active low pressure catalyst for CO_2 conversion to methane. From GIXANES we could already ascertain that the clusters maintain their composition and oxidation state over the cycles. GISAXS results from Figure S8a,b show no evidence that the clusters aggregate under the reaction conditions.

Cu Clusters on Nanostructured Zirconia. Cu_4 clusters on the NS ZrOx support showed a gradual change in the oxidation state of copper, reaching 0.9 at 375 °C from 1.8 at 25 °C. At room temperature the clusters start off as $\text{Cu}(\text{OH})_2$, a component (see Figure S3c) which gradually decreases with increasing temperature and finally vanishes at 175 °C as shown in Figure 2d and for average copper oxidation state in these cluster in Figure 3c. Above this temperature, copper stays in a mixed phase of Cu (20%), Cu_2O (60%), and CuO (20%) as shown in Figure S3c. During cooling the oxidation state starts to increase, reaching 1.5 at room temperature. During the second cycle a similar trend is observed but copper stays more oxidized at 375 °C with an oxidation state of 1 and a higher fraction of CuO component (30%). MCR-ALS for the Cu_4 sample on NS ZrOx suggests a more gradual sample reduction upon heating and a more gradual reoxidation upon cooling in comparison to samples on ALD supports. After reoxidation, the fraction of the metallic phase is found to be lower for the copper tetramer on NS ZrOx.

The methane signal appears at 275 °C and rises to 0.04 at 375 °C and, thus, the same onset temperature for Cu_4 clusters on both ALD and NS ZrOx. However, the activity of Cu_4 on NS ZrOx is 30% higher compared to ALD ZrOx. The most drastic changes are observed during the cooling phase as the activities at 325 °C during the heating and cooling are 0.03 and 0.01

respectively. In the second cycle the maximum activity at 375 °C dropped to 0.01 which is a 75% drop in activity compared to the first ramp. The big change in activity implies a possible restructuring taking place on the NS ZrO_x surface during the heating which leads to quenching the Cu₄ activity. Since, in comparison with studies of similar clusters under different conditions,⁹ no unambiguous indication of noticeable agglomeration of Cu₄ clusters was observed in GISAXS patterns (Figure S8c), a possible explanation for the drop in activity could be that the clusters are less exposed to the reactants, for example by migrating into pores or getting submerged into the surface of NS ZrO_x, as evidenced by the drop of Cu-signal intensity in XPS on the NS ZrO_x support.

Figure 6 shows the Zr 3d and O 1s spectra of NS ZrO_x pristine samples and after thermal treatment without and with clusters.

The fwhm of the Zr 3d peaks is larger than in the previously discussed samples (approximately 2.1 eV). This peak spread is due to the intrinsic nature of the nanostructures, that are

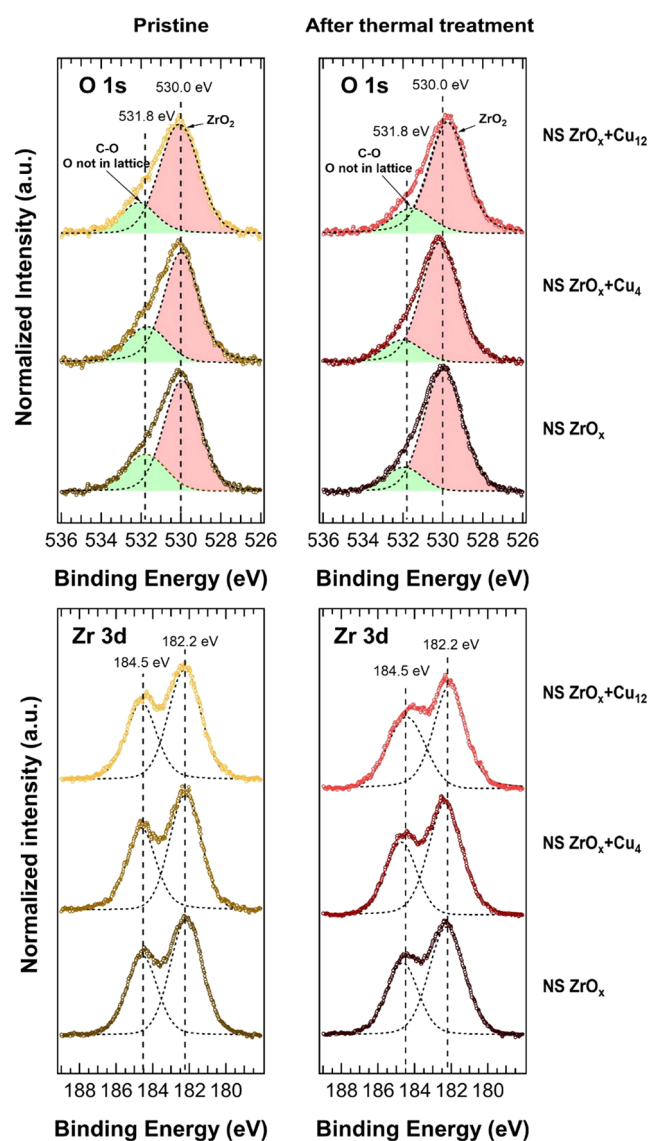


Figure 6. XPS spectra at O 1s (upper panels) and Zr 3d (bottom panels) edges and peaks fitting of NS ZrO_x samples. The spectra of the pristine sample (left column) and after complete thermal process (right column) without and with the Cu clusters are shown.

characterized by nonbulk like bond length relaxation, as well as to the coexistence of cubic crystalline phase and amorphous component in these samples. Thermal treatments promotes the evolution of the nanocrystals toward the monoclinic phase.²⁰ The Zr 3d 5/2 peak for all the samples is located at 182.2 eV with spin-orbit splitting of 2.3 eV. This peak spreading is related to the copresence of the different crystalline phases, and the value of the BE indicates an almost full oxidation of the samples (Zr⁴⁺) as confirmed also by the stoichiometry evaluation. Also at a glance, the deconvoluted oxygen components show an increase of the area under the oxygen in the ZrO₂ lattice and a concomitant decrease of the area of the oxygen not in the regular lattice (531.8 eV). Furthermore, taking into account the porosity and the largest exposed surface of the NS ZrO_x samples with respect to ALD zirconia, the contribution of adventitious species bonded to carbon is expected to be more relevant. In these films there are no silicon fingerprints detectable for the accessible depth with XPS as assessed in the wide scan (not shown); thus no peak at 532.8 eV comes out from the fitting of the oxygen peak. No features interfering with those observed for copper clusters were identified which could have complicated an unambiguous assignment of peaks for the latter samples.

The oxidation state of Cu₁₂ clusters on NS ZrO_x at room temperature is found to be 1.9 (with a composition of Cu(OH)₂, Figure S3d) which drops to 1.1 at 325 °C and does not change any further as the sample is heated up until 375 °C and when subsequently cooled to 225 °C as seen (Figures 2e and 3d). Below 225 °C the oxidation state rises and increases to 1.4 at room temperature. The composition of the clusters is a mixture of Cu, Cu₂O, and CuO in equal proportion (Figure S3d). In the second cycle the oxidation state also shows a drop reaching 1.1 at 375 °C with a similar composition as that in the first cycle, thus indicating reversible changes in the nature of the catalyst. No indication of sintering of Cu₁₂ clusters was observed by GISAXS (Figure S8d) in comparison with earlier studies.⁹

Cu₁₂ becomes active at a temperature of about 175 °C and attains a rate of methane formation r_{CH_4} of 0.05 molecules atom⁻¹ s⁻¹ at 375 °C. The r_{CH_4} is similar at all temperatures recorded during the heating and cooling ramp showing that the changes on the surface of NS ZrO_x does not affect the activity of Cu₁₂ clusters. The activity significantly drops during the second cycle to about 20% of that observed in the first cycle. Interestingly, according to MCR-ALS, the evolution of the oxidation state for Cu₁₂ on NS ZrO_x is very similar to that in Cu₄ on NS ZrO_x. Thus, unlike it was observed for samples on ALD support, the cluster size does not affect significantly the reducibility of the samples on NS ZrO_x.

For nanostructured zirconia the signal at Cu 2p edge was very low also for a possible shadowing and burying effects on Cu clusters due to the rough morphology of the NS ZrO_x substrates. Again, after the described data processing, the Cu appears, as in the case of ALD samples, before and after thermal treatment, mainly in CuO phase for both types of Cu clusters.

Results, obtained by MCR-ALS analysis of Cu K-edge XANES data, for the nanostructured zirconia-supported catalysts are shown in Figure 5c,d. For each of the samples two components (S₁ and S₂) were identified, such that experimental spectra, acquired at different temperatures, can be expressed as linear combinations of S₁ and S₂. Representative fits of experimental XANES spectra with linear combinations of S₁ and S₂ are shown in the Supporting Information, in Figure S7.

Component S₁ resembles the XANES spectrum for metallic copper, while component S₂ can be associated with a spectrum

of oxidized copper species. At the same time, one can see clearly the differences between S_1 and S_2 and XANES data for bulk reference compounds.

The temperature-dependencies of the weight of S_2 component, which can be associated with the fraction of oxidized Cu species, are shown in the insets in Figure 5. Overall, the results obtained via MCR-ALS approach qualitatively agree with the results of conventional LCF analysis. All as-prepared samples are nearly completely oxidized. Upon temperature increase, all samples are reduced. The reduction is more rapid for samples on ALD ZrOx, which are nearly completely metallic at 175–225 °C. Higher reduction temperatures are required for samples on NS ZrOx (325–375 °C). Upon subsequent cooling, all samples are partially reoxidized. For samples on ALD ZrOx reoxidation occurs sharply, when the temperature falls below 175–125 °C. More gradual changes are observed for samples on NS ZrOx. Interestingly, the evolution of the oxidation state for Cu_4 on NS ZrOx and Cu_{12} on NS ZrOx is very similar, suggesting that the cluster size does not affect significantly the reducibility of these samples.

Activation Energy. The activation energy of the Cu clusters on zirconia substrates is evaluated from the Arrhenius plots shown in Figure S9 and are tabulated in Table 1. The r_{CH_4} data

Table 1. Activation Energy for Cu Clusters on Zirconia Supports

catalyst	E_a	
	(kJ/mol)	(eV)
Cu_4 /ALD ZrOx	70.92	0.74
Cu_{12} /ALD ZrOx	15.29	0.16
Cu_4 /NS ZrOx	40.03	0.41
Cu_{12} /NS ZrOx	25.89	0.27

used for calculation are those obtained during the first cycle. Cu_4 on ALD ZrOx has an activation energy of E_a of 70.92 kJ/mol which is comparable to those reported for bulk catalysts for CO_2 methanation;² for example on the Ni(100) surface an E_a of 88.7 kJ/mol has been reported.⁶¹ Cu_4 on Nano ZrOx has higher activity than Cu_4 /ALD ZrOx and has an E_a of 40.03 kJ/mol. A lower E_a of ~40 kJ/mol has recently been reported for Cu nanoparticle doped iron nanocomposites for CO_2 methanation.¹⁰ The Cu_{12} cluster on ALD ZrOx and NS ZrOx has an E_a of 15.29 and 25.89 kJ/mol, respectively, and were also found to be

more active compared to the Cu_4 clusters on the same supports. This low E_a is consistent with the highest activity that we discussed for the Cu_{12} clusters in the previous section.

In passing we note that similar size Cu clusters dispersed on various supports produced different products, ranging from methanol^{7,8,62} to hydrocarbons,^{9,62} thus underlining the pronounced support effects on both activity and selectivity of subnanometer size clusters.

Mechanism and Energy Profile of CO_2 Methanation Reaction. In order to elucidate the reaction mechanism responsible for CO_2 methanation on the Cu_4O_2 cluster at the zirconium oxide support, the DFT calculations have been carried out involving four hydrogenation steps of the reaction. Concerning the model of ZrO support, ZrO_2 subunits have been considered because they are involved in crystalline growth and the subunit $Zr_{12}O_{24}$ has been selected based on findings from previous reactivity studies on Zr oxide.⁶³ The chosen subunit of $Zr_{12}O_{24}$ with Cu_4O_2 has been optimized, and after an extensive search of isomers (cf. Figure S10), the lowest energy structure has been selected as a model. The above-described $Zr_{12}O_{24}$ subunit (Figure 7a) supporting Cu_4O_2 cluster with oxidation number 1 (based on the experimentally determined Cu oxidation state of about 1) with bound HCO_2 (Figure 7b) forms the reactive center $Cu_4O_2Zr_4O_5H-HCO_2$ (Figure 7c). Notice that contribution of the support through the Zr_4O_5 subunit offers functionalization of the copper tetramer with its dual role, since two Cu atoms participate actively in hydrogenation and the other two bind to Zr atoms of the model for support. Mulliken charge analysis provides information that Cu_4 is positively charged.

These results have been obtained based on density functional theory using the B3LYP functional^{64–66} and TZVP AO^{67,68} basis set as well as relativistic effective core potential RECP for Zr atoms.⁶⁹ The minima and transition states along the reaction pathway have been determined employing the Gaussian 16 program package.⁷⁰ In addition, an extensive structural search has been carried out determining the position of CO_2 and H_2 at $Cu_4O_2Zr_{12}O_{24}$ (cf. Figure S11).

The calculated energy profile for CO_2 methanation which involves four hydrogenation steps is presented in Figure 8. The starting point (A) of the reaction is a Cu_4O_2 unit on $Zr_{12}O_{24}$ with CO_2 bound to one of the copper atoms. The first hydrogenation step (B) has been obtained by adding an H_2 molecule, in which one H atom is bound to oxygen and the other one is bridging two Cu atoms gaining 2.04 eV of energy. The barrier for the

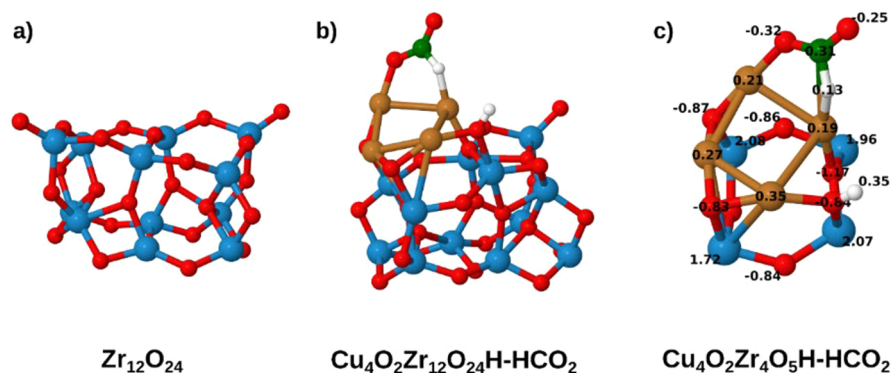


Figure 7. DFT determined structures for (a) $Zr_{12}O_{24}$ subunit, (b) $Cu_4O_2Zr_{12}O_{24}H-HCO_2$ presenting binding of CO_2 and H_2 on $Zr_{12}O_{24}$, and (c) reactive subunit $Cu_4O_2Zr_4O_5H-HCO_2$ evidencing participation of copper cluster and part of support. Mulliken population analysis has been also included. The calculated binding energy of Cu_4O_2 at $Zr_{12}O_{24}$ is 8.14 eV.

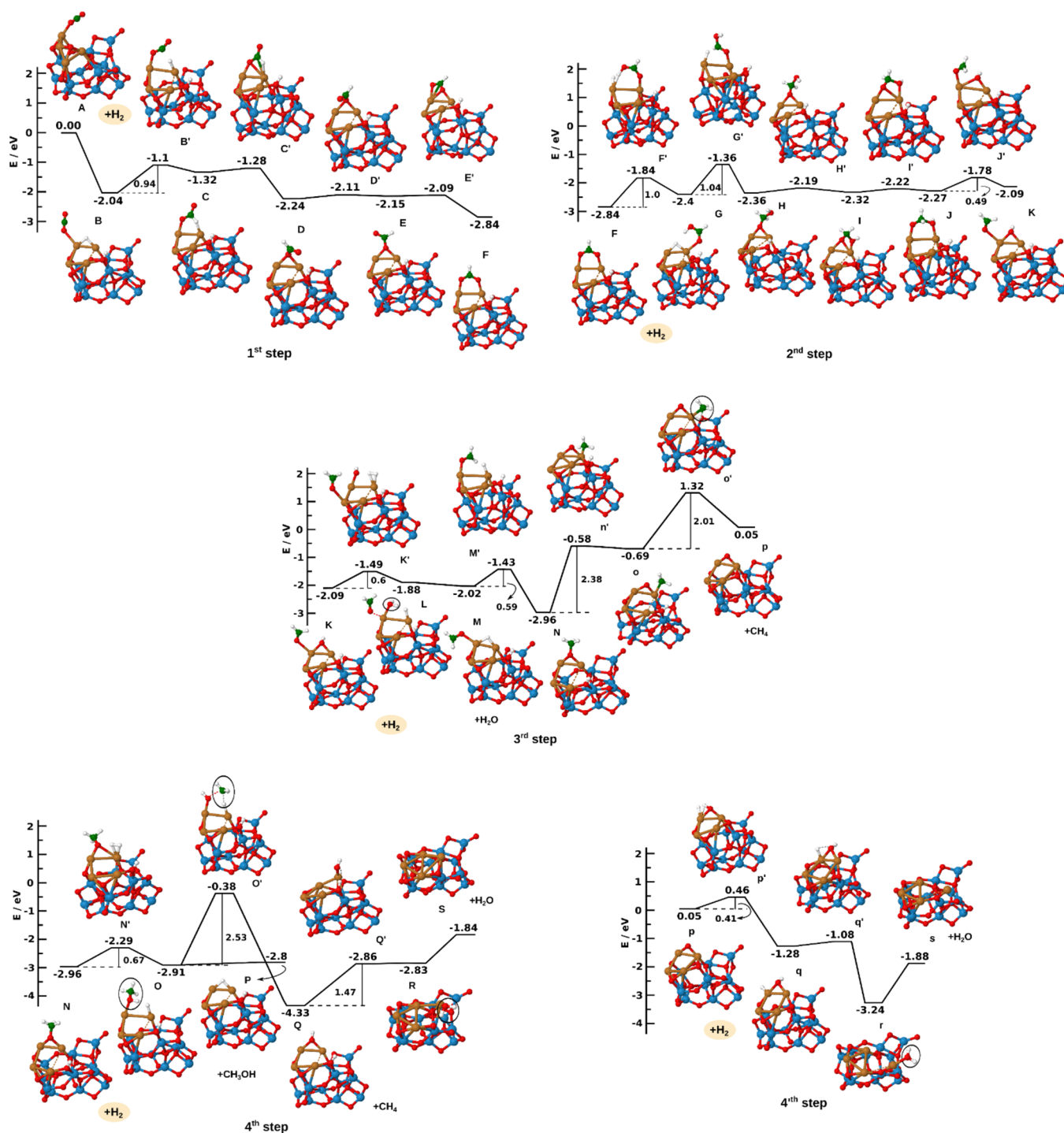


Figure 8. Calculated reaction pathways of CO₂ methanation on an oxidized copper tetramer (Cu₄O₂) supported by Zr₁₂O₂₄ following four steps of hydrogenation (1st step A–F, 2nd step F–K, 3rd K–p, and 4th N–S or 4th p–s). Letters label minima, and letters with primes denote transition states.

activation of CO₂ (B') and formation of HCOO is 0.94 eV. Conformational changes of the HCOO unit located between two Cu atoms lead to a stable configuration of HCOO (F). The subsequent addition of the second H₂ molecule leads to formation of HCOOH (G) over a barrier of 1 eV (F'). In addition, a barrier of 1.04 eV (G') has to be overcome in order to form H₂COOH (H). The steps H–J lead to conformational changes of the H₂COOH unit over small energy barriers, and the activation energy of 0.49 eV (J') is needed for separation of H₂COOH to OCH₂ and OH (K). According to Cu₄O₂ at the

Zr₁₂O₂₄ subunit, methanation of CO₂ proceeds energetically favorable over formation of Cu–HCOO (1st step) and OCH₂ (2nd step). Thus, the reaction mechanism within the first two hydrogenation steps directly involves interaction between two copper atoms with CO₂ and H₂ opening the opportunity to form methane and water within the next two hydrogenation steps described below. In order to consider the possibility of other pathways of hydrogenation, we examined the binding of hydrogen on oxygen instead of carbon. However, the transition state over formation of COOH is considerably higher (2.9 eV, cf.

Figure S12) than the one needed for formation of HCOO (0.94 eV). Therefore, we continued to investigate the methanation reaction following the formation of HCOO shown in Figure 8.

An addition of the third H₂ molecule leads to formation of H₂O (L) and the barrier of 0.59 eV (M') has to be overcome to create OCH₃ (N). Furthermore, the reaction can follow two pathways, one within the third step and the 4'th step (labeled by small letters) and the second one within the fourth step. Along the first branch of the pathway, in order to separate CH₄ two barriers have to be overcome, the first one of 2.38 eV (n') which involves breaking of CO bond by forming Cu₂O and CuCH₃, and the second barrier that requires 2.01 eV (o') forming CH₄ bound to a copper atom. However, this requires 1.32 eV with respect to the starting point of reaction. Along the second branch of the pathway within the fourth step, the H₂ molecule added to the OCH₃ unit forms CH₃OH (O) over a barrier of 0.67 eV (N') and the CH₄ formation originating from Cu-CH₃OH needs to overcome an activation barrier of 2.53 eV (O'). Comparing both branches of the pathway, the second branch is energetically favorable (N-S) and accessible at T = 0 K. The first one is accessible by higher temperatures (N-s) due to a barrier of 2.01 eV, since the corresponding transition state is above starting point of the reaction pathway.

In the fourth step and 4'th step, after separation of CH₄, the formation of water can also be followed by two branches of the pathway. The one along steps p-s requires the energy of 0.46 eV above the starting point of the reaction and therefore is energetically unfavorable at 0 K. The other one involving steps Q'-S is energetically favorable at 0 K. The above-described findings allow us to elucidate the CO₂ methanation reaction and indicate that the mechanism of the CO₂ methanation reaction directly involves two copper atoms from Cu₄O₂ stabilized by a Zr₄O₅ subunit which is accessible to H₂ molecules.

In summary, theoretical modeling based on participation of the Cu₄O₂ subunit and Zr₁₂O₂₄ as a model for support provides the mechanism of reaction, as well as energetically favorable pathways for CO₂ methanation. It is worth mentioning that the participation of the support is essential. Our results fully support experimental findings which showed that Cu₄O₂ at the zirconium oxide surface is responsible for CO₂ methanation. However, in order to design the most efficient reactive center and model support, the consideration of metallic Cu₄ and a bimetallic tetramer interacting with Zr₁₂O₂₄ might also be of interest in the future.

CONCLUSIONS

Cu clusters on zirconia supports form a sintering-resistant catalyst with high activity for CO₂ conversion and high selectivity toward methane formation. The Cu₄/NS ZrOx is about 30% more active compared to Cu₄/ALD ZrOx, whereas Cu₁₂/NS ZrOx is 100% more active compared to Cu₁₂/ALD ZrOx. During CO₂ hydrogenation, copper was found to be partially oxidized. The Cu₄ clusters activate CO₂ at 275 °C, whereas Cu₁₂ does the same already at 175 °C. The activation energy E_a of methane formation on the clusters has been found to be strongly dependent on its size and the support interaction. The subnanometer sized Cu clusters on zirconia supports investigated herein were found to have lower E_a and higher efficiency for methane formation compared to clusters deposited on alumina supports.^{7,8} The zirconia supports with Cu clusters have been found to be one of the more efficient catalyst for CO₂ methanation. The measured r_{CH₄} for Cu₁₂/NS ZrOx makes this catalyst among the best reported so far; however, it was found

that its activity drops during the repeated cycle, most likely due to the possible migration of the clusters into the pores and voids with more limited access to reactants. Preprocessing of the substrate may thus be extremely important so that the catalyst does not lose its catalytic activity and at the same time has higher stability.

The ex situ XPS measurements have assessed the different nature of the zirconia substrates and the fact that copper before and after the process is predominantly in the Cu(I) oxidation state with also a small contribution of Cu(II) in both cases. After the cyclic treatment the possible enhanced burying of the Cu clusters on the NS ZrOx substrate is mirrored by a very low Cu 2p signal which could be related to the observed higher activity for the Cu/NS ZrOx catalysts with respect to the Cu/ALD ZrOx systems, underlining the pronounced effect of the morphology of the support on nanocatalysts' performance, demonstrating the potential of its use in the development of new classes of nanostructured catalysts. With the example of Cu₄, accompanying theoretical investigations provide supporting evidence on its dual role and into the intrinsically high activity of zirconia-supported copper clusters and fundamental insights into the conversion of CO₂ to methane.

Putting this into a broader perspective, this study contributes to the understanding of support effects in catalysis, where selectivity may be switched by altering the support or its morphology.

ASSOCIATED CONTENT

Supporting Information

The Supporting Information is available free of charge at <https://pubs.acs.org/doi/10.1021/acscatal.0c05029>.

Description of cluster synthesis; description of the in situ experiment; AFM image of the support material; mass spectrum of clusters produced; composition of Cu as a function of reaction temperature; XPS spectra of ALD ZrOx; fits of XANES spectra; validation of the MCR-ALS method and its use to fit XANES data; GISAXS cuts; Arrhenius plots; calculated isomers of the catalytic site and its complexes with the reactants; calculated alternative reaction pathway; and supporting references (PDF)

AUTHOR INFORMATION

Corresponding Authors

Paolo Milani – C.I. Ma.I.Na., Dipartimento di Fisica, Università degli Studi di Milano, I-20133 Milano, Italy; Email: Paolo.Milani@mi.infn.it

Stefan Vajda – Materials Science Division, Argonne National Laboratory, Lemont, Illinois 60439, United States; Department of Nanocatalysis, J. Heyrovský Institute of Physical Chemistry, Czech Academy of Sciences, CZ-18223 Prague 8, Czech Republic; orcid.org/0000-0002-1879-2099; Email: stefan.vajda@jh-inst.cas.cz

Authors

Avik Halder – Materials Science Division, Argonne National Laboratory, Lemont, Illinois 60439, United States

Cristina Lenardi – C.I. Ma.I.Na., Dipartimento di Fisica, Università degli Studi di Milano, I-20133 Milano, Italy; orcid.org/0000-0002-5522-6803

Janis Timoshenko – Department of Materials Science and Chemical Engineering, Stony Brook University, Stony Brook, New York 11794, United States

Antonija Mravak – Center of Excellence for Science and Technology - Integration of Mediterranean region (STIM), Faculty of Science, University of Split, CR-21000 Split, Croatia; orcid.org/0000-0002-1252-7390

Bing Yang – Materials Science Division, Argonne National Laboratory, Lemont, Illinois 60439, United States; orcid.org/0000-0003-3515-0642

Lakshmi K Kolipaka – Materials Science Division, Argonne National Laboratory, Lemont, Illinois 60439, United States; orcid.org/0000-0002-1812-4277

Claudio Piazzoni – C.I. Ma.I.Na., Dipartimento di Fisica, Università degli Studi di Milano, I-20133 Milano, Italy

Sönke Seifert – X-ray Science Division, Argonne National Laboratory, Lemont, Illinois 60439, United States

Vlasta Bonacčić-Koutecký – Center of Excellence for Science and Technology - Integration of Mediterranean region (STIM), Faculty of Science, University of Split, CR-21000 Split, Croatia; Interdisciplinary Center for Advanced Science and Technology (ICAST), University of Split, CR-21000 Split, Croatia; Chemistry Department, Humboldt University of Berlin, D-12489 Berlin, Germany

Anatoly I. Frenkel – Department of Materials Science and Chemical Engineering, Stony Brook University, Stony Brook, New York 11794, United States; Division of Chemistry, Brookhaven National Laboratory, Upton, New York 11973, United States; orcid.org/0000-0002-5451-1207

Complete contact information is available at:
<https://pubs.acs.org/10.1021/acscatal.0c05029>

Author Contributions

◆ A.H., C.L., J.T., and A.M. are equally contributing (first) authors.

Notes

The authors declare no competing financial interest.

ACKNOWLEDGMENTS

The authors thank Dr. Alex Martinson for discussing the chemistry of the synthesis of the ALD ZrO_x films, Dr. Michael Pellin for preparing the ALD coating, and Dr. Francesca Borghi for AFM characterization of the nanostructured zirconia films. V.B.K. and A.M. acknowledge computational facilities of the HPC computer within the STIM-REI project, Doctoral study of Biophysics at University of Split as well as Prof. Miroslav Radman at MedILS and Split-Dalmatia County for support. The work at Argonne was supported by the U.S. Department of Energy, BES Materials Sciences under Contract No. DEAC02-06CH11357 with U Chicago Argonne, LLC, operator of Argonne National Laboratory. The work at the Advance Photon Source (SS, beamline 12-ID-C) was supported by the U.S. Department of Energy, Scientific User Facilities under Contract No. DEAC02-06CH11357 with U Chicago Argonne, LLC, operator of Argonne National Laboratory. XAS analysis work of A.I.F. was supported in part by the Catalysis Center for Energy Innovation, an Energy Frontier Research Center funded by the U.S. Department of Energy, Office of Science, Office of Basic Energy Sciences under Award No. DE-SC0001004. The research by A.M. and V.B.K. was partially supported by the project STIM-REI, Contract No. KK.01.1.1.01.0003, funded by the European Union through the European Regional Develop-

ment Fund—the Operational Programme Competitiveness and Cohesion 2014–2020 (KK.01.1.1.01). S.V. also acknowledges support from the European Union's Horizon 2020 research and innovation programme under grant agreement No 810310, which corresponds to the J. Heyrovsky Chair project ("ERA Chair at J. Heyrovský Institute of Physical Chemistry AS CR – The institutional approach towards ERA") during the finalization of the paper. The funders had no role in the preparation of the article.

REFERENCES

- (1) Aresta, M.; Dibenedetto, A.; Angelini, A. Catalysis for the Valorization of Exhaust Carbon: from CO₂ to Chemicals, Materials, and Fuels Technological Use of CO₂. *Chem. Rev.* **2014**, *114* (3), 1709–1742.
- (2) Wei, W.; Jinlong, G. Methanation of carbon dioxide: an overview. *Front. Chem. Sci. Eng.* **2011**, *5* (1), 2–10.
- (3) Ahouari, H.; Soualah, A.; Le Valant, A.; Pinard, L.; Magnoux, P.; Pouilloux, Y. Methanol synthesis from CO₂ hydrogenation over copper based catalysts. *React. Kinet., Mech. Catal.* **2013**, *110* (1), 131–145.
- (4) Behrens, M.; Studt, F.; Kasatkin, I.; Kühn, S.; Hävecker, M.; Abild-Pedersen, F.; Zander, S.; Girgsdies, F.; Kurr, P.; Knief, B.-L.; Tovar, M.; Fischer, R. W.; Nørskov, J. K.; Schlögl, R. The Active Site of Methanol Synthesis over Cu/ZnO/Al₂O₃ Industrial Catalysts. *Science* **2012**, *336* (6083), 893–897.
- (5) Graciani, J.; Mudiyansele, K.; Xu, F.; Baber, A. E.; Evans, J.; Senanayake, S. D.; Stacchiola, D. J.; Liu, P.; Hrbek, J.; Sanz, J. F.; Rodriguez, J. A. Highly active copper-ceria and copper-ceria-titania catalysts for methanol synthesis from CO₂. *Science* **2014**, *345* (6196), 546–550.
- (6) Waugh, K. C. Methanol Synthesis. *Catal. Today* **1992**, *15* (1), 51–75.
- (7) Liu, C.; Yang, B.; Tyo, E.; Seifert, S.; DeBartolo, J.; von Issendorff, B.; Zapol, P.; Vajda, S.; Curtiss, L. A. Carbon Dioxide Conversion to Methanol over Size-Selected Cu₄ Clusters at Low Pressures. *J. Am. Chem. Soc.* **2015**, *137* (27), 8676–8679.
- (8) Yang, B.; Liu, C.; Halder, A.; Tyo, E. C.; Martinson, A. B. F.; Seifert, S.; Zapol, P.; Curtiss, L. A.; Vajda, S. Copper Cluster Size Effect in Methanol Synthesis from CO₂. *J. Phys. Chem. C* **2017**, *121* (19), 10406–10412.
- (9) Halder, A.; Kioseoglou, J.; Yang, B.; Kolipaka, K. L.; Seifert, S.; Ilavsky, J.; Pellin, M.; Sowwan, M.; Grammatikopoulos, P.; Vajda, S. Nanoassemblies of ultrasmall clusters with remarkable activity in carbon dioxide conversion into C1 fuels. *Nanoscale* **2019**, *11* (11), 4683–4687.
- (10) Halder, A.; Kilianová, M.; Yang, B.; Tyo, E. C.; Seifert, S.; Prucek, R.; Panáček, A.; Suchomel, P.; Tomanec, O.; Gosztola, D. J.; Milde, D.; Wang, H.-H.; Kvítek, L.; Zbořil, R.; Vajda, S. Highly efficient Cu-decorated iron oxide nanocatalyst for low pressure CO₂ conversion. *Appl. Catal., B* **2018**, *225*, 128–138.
- (11) Gasser, D.; Baiker, A. Hydrogenation of carbon dioxide over copper—zirconia catalysts prepared by in-situ activation of amorphous copper—zirconium alloy. *Appl. Catal.* **1989**, *48* (2), 279–294.
- (12) Koeppel, R. A.; Baiker, A.; Schild, C.; Wokaun, A. Effect of Preparation Variables on Catalytic Behaviour of Copper/Zirconia Catalysts for the Synthesis of Methanol from Carbon Dioxide. In *Stud. Surf. Sci. Catal.*; Poncelet, G., Jacobs, P. A., Grange, P., Delmon, B., Eds.; Elsevier: 1991; Vol. 63, pp 59–68.
- (13) Wang, Y. H.; Gao, W. G.; Wang, H.; Zheng, Y. E.; Na, W.; Li, K. Z. Structure-activity relationships of Cu-ZrO₂ catalysts for CO₂ hydrogenation to methanol: interaction effects and reaction mechanism. *RSC Adv.* **2017**, *7* (14), 8709–8717.
- (14) Samson, K.; Śliwa, M.; Socha, R. P.; Góra-Marek, K.; Mucha, D.; Rutkowska-Zbik, D.; Paul, J. F.; Ruggiero-Mikołajczyk, M.; Grabowski, R.; Słoczyński, J. Influence of ZrO₂ Structure and Copper Electronic State on Activity of Cu/ZrO₂ Catalysts in Methanol Synthesis from CO₂. *ACS Catal.* **2014**, *4* (10), 3730–3741.

- (15) Tada, S.; Watanabe, F.; Kiyota, K.; Shimoda, N.; Hayashi, R.; Takahashi, M.; Nariyuki, A.; Igarashi, A.; Satokawa, S. Ag addition to CuO-ZrO₂ catalysts promotes methanol synthesis via CO₂ hydrogenation. *J. Catal.* **2017**, *351*, 107–118.
- (16) Tada, S.; Katagiri, A.; Kiyota, K.; Honma, T.; Kamei, H.; Nariyuki, A.; Uchida, S.; Satokawa, S. Cu Species Incorporated into Amorphous ZrO₂ with High Activity and Selectivity in CO₂-to-Methanol Hydrogenation. *J. Phys. Chem. C* **2018**, *122* (10), 5430–5442.
- (17) Din, I. U.; Shaharun, M. S.; Naeem, A.; Tasleem, S.; Rafie Johan, M. Carbon nanofibers based copper/zirconia catalysts for carbon dioxide hydrogenation to methanol: Effect of copper concentration. *Chem. Eng. J.* **2018**, *334*, 619–629.
- (18) Rungtaweeworani, B.; Baek, J.; Araujo, J. R.; Archanjo, B. S.; Choi, K. M.; Yaghi, O. M.; Somorjai, G. A. Copper Nanocrystals Encapsulated in Zr-based Metal–Organic Frameworks for Highly Selective CO₂ Hydrogenation to Methanol. *Nano Lett.* **2016**, *16* (12), 7645–7649.
- (19) Riha, S. C.; Jin, S.; Baryshev, S. V.; Thimsen, E.; Wiederrecht, G. P.; Martinson, A. B. F. Stabilizing Cu₂S for Photovoltaics One Atomic Layer at a Time. *ACS Appl. Mater. Interfaces* **2013**, *5* (20), 10302–10309.
- (20) Borghi, F.; Sogne, E.; Lenardi, C.; Podestà, A.; Merlini, M.; Ducati, C.; Milani, P. Cluster-assembled cubic zirconia films with tunable and stable nanoscale morphology against thermal annealing. *J. Appl. Phys.* **2016**, *120* (5), 055302.
- (21) Borghi, F.; Podestà, A.; Piazzoni, C.; Milani, P. Growth Mechanism of Cluster-Assembled Surfaces: From Submonolayer to Thin-Film Regime. *Phys. Rev. Appl.* **2018**, *9* (4), 044016.
- (22) Galli, A.; Maffioli, E.; Sogne, E.; Moretti, S.; Di Cairano, E. S.; Negri, A.; Nonnis, S.; Norata, G. D.; Bonacina, F.; Borghi, F.; Podestà, A.; Bertuzzi, F.; Milani, P.; Lenardi, C.; Tedeschi, G.; Perego, C. Cluster-assembled zirconia substrates promote long-term differentiation and functioning of human islets of Langerhans. *Sci. Rep.* **2018**, *8* (1), 9979.
- (23) Chen, H.-Y. T.; Tosoni, S.; Pacchioni, G. Hydrogen Adsorption, Dissociation, and Spillover on Ru₁₀ Clusters Supported on Anatase TiO₂ and Tetragonal ZrO₂ (101) Surfaces. *ACS Catal.* **2015**, *5* (9), 5486–5495.
- (24) Timoshenko, J.; Halder, A.; Yang, B.; Seifert, S.; Pellin, M. J.; Vajda, S.; Frenkel, A. I. Subnanometer Substructures in Nano-assemblies Formed from Clusters under a Reactive Atmosphere Revealed Using Machine Learning. *J. Phys. Chem. C* **2018**, *122* (37), 21686–21693.
- (25) Tyo, E. C.; Vajda, S. Catalysis by clusters with precise numbers of atoms. *Nat. Nanotechnol.* **2015**, *10*, 577.
- (26) Veselovskaya, J. V.; Parunin, P. D.; Okunev, A. G. Catalytic process for methane production from atmospheric carbon dioxide utilizing Renew Energy. *Catal. Today* **2017**, *298*, 117–123.
- (27) Al-Swai, B. M.; Osman, N. B.; Abdullah, B. Catalytic performance of Ni/MgO catalyst in methane dry reforming. *AIP Conf. Proc.* **2017**, *1891* (1), 020028.
- (28) Themelis, N. J.; Ulloa, P. A. Methane generation in landfills. *Renewable Energy* **2007**, *32* (7), 1243–1257.
- (29) Klassen, V.; Blifernez-Klassen, O.; Wibberg, D.; Winkler, A.; Kalinowski, J.; Posten, C.; Kruse, O. Highly efficient methane generation from untreated microalgae biomass. *Biotechnol. Biofuels* **2017**, *10* (1), 186.
- (30) Fuertez, J.; Nguyen, V.; McLennan, J. D.; Adams, D. J.; Han, K.-B.; Sparks, T. D. Optimization of biogenic methane production from coal. *Int. J. Coal Geol.* **2017**, *183*, 14–24.
- (31) Ahlberg-Eliasson, K.; Nadeau, E.; Levén, L.; Schnürer, A. Production efficiency of Swedish farm-scale biogas plants. *Biomass Bioenergy* **2017**, *97*, 27–37.
- (32) Borole, A. P.; Klasson, K. T.; Ridenour, W.; Holland, J.; Karim, K.; Al-Dahhan, M. H. Methane Production in a 100-L Upflow Bioreactor by Anaerobic Digestion of Farm Waste. In *Twenty-Seventh Symposium on Biotechnology for Fuels and Chemicals*; McMillan, J. D., Adney, W. S., Mielenz, J. R., Klasson, K. T., Eds.; Humana Press: Totowa, NJ, 2006; pp 887–896.
- (33) Wegner, K.; Piseri, P.; Tafreshi, H. V.; Milani, P. Cluster beam deposition: a tool for nanoscale science and technology. *J. Phys. D: Appl. Phys.* **2006**, *39* (22), R439–R459.
- (34) Yin, C.; Tyo, E.; Kuchta, K.; von Issendorff, B.; Vajda, S. Atomically precise (catalytic) particles synthesized by a novel cluster deposition instrument. *J. Chem. Phys.* **2014**, *140* (17), 174201.
- (35) Lee, S.; Lee, B.; Seifert, S.; Vajda, S.; Winans, R. E. Simultaneous measurement of X-ray small angle scattering, absorption and reactivity: A continuous flow catalysis reactor. *Nucl. Instrum. Methods Phys. Res., Sect. A* **2011**, *649* (1), 200–203.
- (36) Lei, Y.; Mehmood, F.; Lee, S.; Greeley, J.; Lee, B.; Seifert, S.; Winans, R. E.; Elam, J. W.; Meyer, R. J.; Redfern, P. C.; Teschner, D.; Schlögl, R.; Pellin, M. J.; Curtiss, L. A.; Vajda, S. Increased Silver Activity for Direct Propylene Epoxidation via Subnanometer Size Effects. *Science* **2010**, *328* (5975), 224–228.
- (37) Martini, A.; Borfecchia, E. Spectral Decomposition of X-ray Absorption Spectroscopy Datasets: Methods and Applications. *Crystals* **2020**, *10* (8), 664.
- (38) Lee, B.; Seifert, S.; Riley, S. J.; Tikhonov, G.; Tomczyk, N. A.; Vajda, S.; Winans, R. E. Anomalous grazing incidence small-angle x-ray scattering studies of platinum nanoparticles formed by cluster deposition. *J. Chem. Phys.* **2005**, *123* (7), 074701.
- (39) Keshari, A. K.; Pandey, A. C. Size and Distribution: A Comparison of XRD, SAXS and SANS Study of II–VI Semiconductor Nanocrystals. *J. Nanosci. Nanotechnol.* **2008**, *8* (3), 1221–1227.
- (40) Wyrzgol, S. A.; Schafer, S.; Lee, S.; Lee, B.; Vece, M. D.; Li, X.; Seifert, S.; Winans, R. E.; Stutzmann, M.; Lercher, J. A.; Vajda, S. Combined TPRx, in situ GISAXS and GIXAS studies of model semiconductor-supported platinum catalysts in the hydrogenation of ethene. *Phys. Chem. Chem. Phys.* **2010**, *12* (21), 5585–5595.
- (41) Ilavsky, J.; Jemian, P. R. Irena: tool suite for modeling and analysis of small-angle scattering. *J. Appl. Crystallogr.* **2009**, *42* (2), 347–353.
- (42) Passalacqua, R.; Parathoner, S.; Centi, G.; Halder, A.; Tyo, E. C.; Yang, B.; Seifert, S.; Vajda, S. Electrochemical behaviour of naked sub-nanometre sized copper clusters and effect of CO₂. *Catal. Sci. Technol.* **2016**, *6* (18), 6977–6985.
- (43) Alayon, E. M. C.; Nachttegaal, M.; Bodi, A.; van Bokhoven, J. A. Reaction Conditions of Methane-to-Methanol Conversion Affect the Structure of Active Copper Sites. *ACS Catal.* **2014**, *4* (1), 16–22.
- (44) Felten, J.; Hall, H.; Jaumot, J.; Tauler, R.; de Juan, A.; Gorzsás, A. Vibrational spectroscopic image analysis of biological material using multivariate curve resolution–alternating least squares (MCR-ALS). *Nat. Protoc.* **2015**, *10* (2), 217–240.
- (45) Ruckebusch, C.; Blanchet, L. Multivariate curve resolution: a review of advanced and tailored applications and challenges. *Anal. Chim. Acta* **2013**, *765*, 28–36.
- (46) Cassinelli, W. H.; Martins, L.; Passos, A. R.; Pulcinelli, S. H.; Santilli, C. V.; Rochet, A.; Briois, V. Multivariate curve resolution analysis applied to time-resolved synchrotron X-ray Absorption Spectroscopy monitoring of the activation of copper alumina catalyst. *Catal. Today* **2014**, *229*, 114–122.
- (47) Voronov, A.; Urakawa, A.; Beek, W. v.; Tsakoumis, N. E.; Emerich, H.; Rønning, M. Multivariate curve resolution applied to in situ X-ray absorption spectroscopy data: An efficient tool for data processing and analysis. *Anal. Chim. Acta* **2014**, *840*, 20–27.
- (48) Nayak, C.; Bhattacharyya, D.; Jha, S. N.; Sahoo, N. K. In Situ XAS Study on Growth of PVP-Stabilized Cu Nanoparticles. *ChemistrySelect* **2018**, *3* (25), 7370–7377.
- (49) Frenkel, A. I.; Kleifeld, O.; Wasserman, S. R.; Sagi, I. Phase speciation by extended x-ray absorption fine structure spectroscopy. *J. Chem. Phys.* **2002**, *116* (21), 9449–9456.
- (50) Wang, X.; Hanson, J. C.; Frenkel, A. I.; Kim, J.-Y.; Rodriguez, J. A. Time-resolved Studies for the Mechanism of Reduction of Copper Oxides with Carbon Monoxide: Complex Behavior of Lattice Oxygen

and the Formation of Suboxides. *J. Phys. Chem. B* **2004**, *108* (36), 13667–13673.

(51) Wang, Q.; Hanson, J. C.; Frenkel, A. I. Solving the structure of reaction intermediates by time-resolved synchrotron x-ray absorption spectroscopy. *J. Chem. Phys.* **2008**, *129* (23), 234502.

(52) Nong, S.; Dong, W.; Xiao, Y.; Riaz, M. S.; Dong, C.; Zhao, Y.; Liu, Z.; Wang, R.; Huang, F. Highly Hydroxylated Porous Nanozirconia for Complete Trace Cr(VI) Removal. *ACS Appl. Nano Mater.* **2020**, *3* (4), 3315–3322.

(53) Scotti, N.; Bossola, F.; Zaccheria, F.; Ravasio, N. Copper–Zirconia Catalysts: Powerful Multifunctional Catalytic Tools to Approach Sustainable Processes. *Catalysts* **2020**, *10* (2), 168.

(54) Pauly, N.; Tougaard, S.; Yubero, F. Determination of the Cu 2p primary excitation spectra for Cu, Cu₂O and CuO. *Surf. Sci.* **2014**, *620*, 17–22.

(55) Timoshenko, J.; Lu, D.; Lin, Y.; Frenkel, A. I. Supervised Machine-Learning-Based Determination of Three-Dimensional Structure of Metallic Nanoparticles. *J. Phys. Chem. Lett.* **2017**, *8* (20), 5091–5098.

(56) Weatherbee, G. D.; Bartholomew, C. H. Hydrogenation of CO₂ on group VIII metals: I Specific activity of NiSiO₂. *J. Catal.* **1981**, *68* (1), 67–76.

(57) Chang, F.-W.; Hsiao, T.-J.; Shih, J.-D. Hydrogenation of CO₂ over a Rice Husk Ash Supported Nickel Catalyst Prepared by Deposition–Precipitation. *Ind. Eng. Chem. Res.* **1998**, *37* (10), 3838–3845.

(58) Chang, F.-W.; Tsay, M.-T.; Liang, S.-P. Hydrogenation of CO₂ over nickel catalysts supported on rice husk ash prepared by ion exchange. *Appl. Catal., A* **2001**, *209* (1), 217–227.

(59) Bebelis, S.; Karasali, H.; Vayenas, C. G. Electrochemical promotion of CO₂ hydrogenation on Rh/YSZ electrodes. *J. Appl. Electrochem.* **2008**, *38* (8), 1127–1133.

(60) Papaioannou, E. I.; Souentie, S.; Hammad, A.; Vayenas, C. G. Electrochemical promotion of the CO₂ hydrogenation reaction using thin Rh, Pt and Cu films in a monolithic reactor at atmospheric pressure. *Catal. Today* **2009**, *146* (3), 336–344.

(61) Peebles, D. E.; Goodman, D. W.; White, J. M. Methanation of carbon dioxide on nickel(100) and the effects of surface modifiers. *J. Phys. Chem.* **1983**, *87* (22), 4378–4387.

(62) Yang, B.; Yu, X.; Halder, A.; Zhang, X.; Zhou, X.; Mannie, G. J. A.; Tyo, E.; Pellin, M. J.; Seifert, S.; Su, D.; Vajda, S. Dynamic Interplay between Copper Tetramers and Iron Oxide Boosting CO₂ Conversion to Methanol and Hydrocarbons under Mild Conditions. *ACS Sustainable Chem. Eng.* **2019**, *7* (17), 14435–14442.

(63) Nöbšler, M.; Mitrić, R.; Bonačić-Koutecký, V. Binary Neutral Metal Oxide Clusters with Oxygen Radical Centers for Catalytic Oxidation Reactions: From Cluster Models Toward Surfaces. *J. Phys. Chem. C* **2012**, *116* (21), 11570–11574.

(64) Becke, A. D. Density-functional exchange-energy approximation with correct asymptotic behavior. *Phys. Rev. A: At., Mol., Opt. Phys.* **1988**, *38* (6), 3098–3100.

(65) Becke, A. D. Density-functional thermochemistry III The role of exact exchange. *J. Chem. Phys.* **1993**, *98* (7), 5648–5652.

(66) Lee, C.; Yang, W.; Parr, R. G. Development of the Colle-Salvetti correlation-energy formula into a functional of the electron density. *Phys. Rev. B: Condens. Matter Mater. Phys.* **1988**, *37* (2), 785–789.

(67) Schäfer, A.; Huber, C.; Ahlrichs, R. Fully optimized contracted Gaussian basis sets of triple zeta valence quality for atoms Li to Kr. *J. Chem. Phys.* **1994**, *100* (8), 5829–5835.

(68) Eichkorn, K.; Weigend, F.; Treutler, O.; Ahlrichs, R. Auxiliary basis sets for main row atoms and transition metals and their use to approximate Coulomb potentials. *Theor. Chem. Acc.* **1997**, *97* (1), 119–124.

(69) Andrae, D.; Häußermann, U.; Dolg, M.; Stoll, H.; Preuß, H. Energy-adjusted ab initio pseudopotentials for the second and third row transition elements. *Theor. Chim. Acta* **1990**, *77* (2), 123–141.

(70) Frisch, M. J.; et al. *Gaussian 16*, revision C.01; Gaussian Inc.: Wallingford, CT, 2016.